applied sciences

MDPI

Article

From Analytical to Discrete Image-Based Contour Hologram Synthesis: A Comparative Analysis

Alejandra Serrano-Trujillo *, José Jaime Esqueda-Elizondo, Diego Armando Trujillo-Toledo and Laura Jiménez-Beristáin

Facultad de Ciencias Químicas e Ingeniería, Universidad Autónoma de Baja California, Tijuana 22427, Mexico; jjesqueda@uabc.edu.mx (J.J.E.-E.); dtrujillotoledo@uabc.edu.mx (D.A.T.-T.); ljimenezb@uabc.edu.mx (L.J.-B.)
* Correspondence: aserrano11@uabc.edu.mx

Abstract

A computational comparison between analytical and discrete image-based formulations for contour hologram synthesis is presented. The analytical approach relies on contour parameterization and Fourier-descriptor reconstruction to compute the phase accumulated along a closed contour, while the proposed discrete image-based approach performs contour extraction and phase accumulation directly on sampled spatial grids without explicit parametric modeling. Both methods were implemented under identical computational conditions and evaluated through numerical propagation in the Fraunhofer regime using representative contour geometries of increasing spatial complexity. Reconstruction quality was assessed using the Structural Similarity Index (SSIM), phase topology analysis, and hologram generation time measurements. Results show that both approaches successfully reconstruct the target contours while preserving the prescribed topological charge and phase winding behavior. High structural fidelity was obtained in all cases, with SSIM values above 0.93. The discrete image-based approach consistently produced slightly higher similarity values and achieved substantial reductions in computational cost, with speed-up factors ranging from approximately 120× to more than 1600×, depending on contour complexity. These results demonstrate that direct operation on sampled contour representations provides an efficient alternative to analytical contour parameterization while maintaining reconstruction quality and topological consistency.

Keywords: computer-generated holography; contour hologram synthesis; structured light; orbital angular momentum; discrete image-based formulation

Check for updates

Academic Editors: Nunzio Cennamo, Andrés Márquez and Stefano Toldo

Received: 28 May 2026
Revised: 4 July 2026
Accepted: 7 July 2026
Published: 9 July 2026

1. Introduction

The generation of structured light beams with tailored amplitude and phase distributions has become a central aspect of modern photonics, enabling applications in optical manipulation, microscopy, high-capacity communications, and quantum information processing [1–3]. In particular, optical fields carrying orbital angular momentum (OAM) have attracted significant attention due to their helical phase structure and associated topological charge, which provide an additional degree of freedom for encoding and manipulating information [4]. Advances in beam-shaping techniques have enabled the synthesis of complex optical fields using spatial light modulators (SLMs), diffractive optical elements and computational holography frameworks [5–7].

Computer-generated holography (CGH) has emerged as a powerful tool for designing structured optical fields by encoding a desired wavefront into a phase distribution that can be reconstructed through diffraction [8]. However, CGH remains computationally demanding, particularly when accurate reconstruction quality must be achieved under practical sampling and propagation constraints. This limitation has motivated the development of iterative, non-iterative, hardware-accelerated, and learning-based hologram generation strategies [9–16].

Several recent approaches have focused on reducing CGH computation time. Experimental evaluations using DMD-based amplitude and phase modulation have also demonstrated reconstruction quality under practical optical conditions [17]. GPU acceleration, low-precision implementations, and lookup-table-based strategies have been explored to improve the efficiency of hologram generation [12,13]. Non-iterative phase-only hologram generation and gradient-based optimization have also been proposed to reduce the computational challenge while maintaining reconstruction quality [9–11]. In parallel, CGH based on deep learning has been widely investigated as a means of approximating the inverse hologram generation problem, although such approaches may require large datasets and can exhibit generalization limitations when applied to arbitrary geometries [14–16].

CGH methods based on contours and analytical formulations are particularly relevant for hologram synthesis from geometric primitives. Recent work has reviewed CGH fundamentals based on contour representations, including analytical affine transformation methods, and has shown that the computational cost of polygon and contour representations remains an important issue in practical hologram generation [18]. Accelerated CGH methods based on geometric primitives, using look-up tables and principal component analysis have also been reported, demonstrating the relevance of reducing repeated analytical computations in geometry-based hologram synthesis [13]. Related analytical affine transformation methods further show that efficient handling of polygonal or contour-based data is a continuing topic in CGH research [19].

Other recent methods have addressed hologram acceleration from different perspectives, including fast phase optimization, sparse Fourier holograms, Monte Carlo-based CGH strategies, and phase-seeded point-based approaches [20–23]. For example, the Instant-SFH method proposed by Li et al. employs a non-iterative sparse Fourier strategy to achieve substantial computational acceleration while preserving image quality metrics [21]. These methods show that computation time can be significantly reduced in hologram generation for general applications. Statistical approaches based on Monte Carlo sampling have also been explored as alternative strategies for reducing computational cost in CGH [22]. However, their objectives differ from the present work, which focuses specifically on how the representation of a closed contour affects hologram synthesis performance when analytical and discrete image-based formulations are compared under identical propagation and evaluation conditions.

In parallel, the synthesis of vortex beams and structured light fields with arbitrary spatial distributions has gained increasing attention. Techniques based on phase engineering and optical vortex design have enabled complex light field generation, although many approaches remain dependent on predefined beam models or geometry-specific parameterizations [4,24–26]. This highlights the need for flexible contour-based approaches capable of handling arbitrary shapes without requiring explicit continuous parameterization.

Discrete image-based formulations provide an alternative route for contour hologram synthesis. In these approaches, binary masks and extracted contour pixels are used directly as sampled spatial representations of the target geometry, without requiring explicit symbolic parameterization or integration in the continuous domain [27–29]. This strategy is consistent with established digital image processing methodologies in which sampled spatial representations and edge-based features are used for structural analysis and reconstruction assessment [27,28].

A key aspect in evaluating reconstructed optical fields is the selection of appropriate quality metrics. The Structural Similarity Index (SSIM) is particularly useful for contour-based comparisons because it evaluates structural agreement and local spatial organization rather than only pointwise intensity differences [30]. This characteristic is especially relevant in the present study, where the objective is not to reproduce grayscale scenes but to evaluate the preservation of contour geometry and encoded phase characteristics. For this reason, SSIM is used together with phase topology inspection and hologram generation time measurements. Many studies focus on accelerating CGH through hardware optimization, deep learning, Monte Carlo sampling, or fast numerical algorithms [12–16,20–22,31,32]. However, comparatively less attention has been paid to how the mathematical representation of the contour itself influences hologram generation. In particular, a systematic comparison between continuous analytical parameterizations and fully discrete image-based formulations remains limited. Therefore, it is still necessary to evaluate how these two representation strategies affect reconstruction quality, topological preservation, and processing time under identical propagation conditions.

The main contributions of this work are (i) a discrete image-based formulation for contour hologram synthesis that avoids explicit continuous parameterization; (ii) a systematic comparison with an analytical contour-based formulation under identical computational conditions; and (iii) a quantitative evaluation of structural fidelity (SSIM), topological consistency, and hologram generation time using representative contour geometries. By isolating the role of contour representation from other acceleration strategies, this study provides insight into the trade-off between reconstruction fidelity and computational efficiency in contour hologram synthesis.

2. Materials and Methods

This section describes the analytical and discrete image-based formulations used for contour hologram synthesis, together with the numerical implementation and evaluation procedure adopted for their comparison. Both approaches are implemented under identical computational conditions, including spatial sampling, the propagation model, and input geometries, to ensure a consistent and reproducible assessment of their performance.

2.1. Analytical Formulation

The analytical formulation represents the target contour as a continuous closed curve reconstructed from the ordered contour points extracted from the binary input geometry. The contour is described through a parametric representation, allowing phase accumulation to be evaluated along a continuous trajectory [24]. Let the contour be described by

$$r(t) = (x(t), y(t)), \tag{1}$$

with $t \in [0,\ T]$, defining a continuous traversal of the closed path. The corresponding phase accumulation along the contour is expressed as

$$\phi_{contour} \propto \oint (x\,dy - y\,dx), \tag{2}$$

which yields the accumulated phase around the curve. The topological charge ℓ is determined by the total phase winding, expressed as [4]

$$\ell = \frac{1}{2\pi}\oint \nabla\phi \cdot dl. \tag{3}$$

By introducing the parametric representation, the contour integral can be rewritten as

$$\phi_{contour} \propto \int_0^T \left(x(t)\frac{dy}{dt} - y(t)\frac{dx}{dt} \right) dt. \tag{4}$$

In practice, the contour is discretized into an ordered sequence of points, and the integral is approximated numerically. This requires reconstruction of the parametric representation from discrete contour data, obtained through edge detection and contour extraction techniques commonly used in digital image processing [27,28]. Numerical differentiation and integration are then applied to estimate the phase distribution. In this study, the analytical formulation serves as the reference approach against which the discrete image-based formulation is evaluated.

The contour parameterization is reconstructed using Fourier descriptor representation obtained from the ordered contour sequence [18,19]. To obtain a compact representation, only the harmonics required to retain approximately 95% of the cumulative spectral energy were used. This preserves the dominant contour information while reducing high-frequency fluctuations. This threshold was selected as a compromise between contour fidelity and computational complexity, preserving the dominant geometric features while limiting the number of Fourier coefficients required for reconstruction. The implementation therefore requires contour parameterization followed by derivative estimation and numerical integration, which may increase computational cost for geometries with high spatial complexity.

2.2. Discrete Image-Based Formulation

As summarized in Figure 1, the discrete image-based formulation replaces contour parameterization with direct processing of sampled contour pixels extracted from the binary input geometry [27–29]. The input geometry is defined as a binary mask $M(x,y)$, where foreground pixels represent the target contour. From this representation, the contour is extracted as an ordered sequence of edge pixels

$$\mathrm{P} = \{(x_i, y_i)\}_{i=1}^{N}, \tag{5}$$

forming a closed path suitable for phase accumulation. To ensure consistency in phase computation, the extracted contour is mapped to a centered Cartesian coordinate system by subtracting the image midpoint $\left(\frac{N_x}{2}, \frac{N_y}{2}\right)$, where $N_x = N_y = 512$. The contour ordering enables discrete traversal of the geometry while preserving local spatial relationships between neighboring contour points. The phase associated with a prescribed topological charge ℓ is computed by distributing the total phase winding $2\pi\ell$ along the contour length. Let s_i denote the cumulative arc length from the starting contour point to the i-th contour point, and let S_{total} denote the total contour perimeter. The phase assigned to each contour point is defined as

$$\phi_i = \frac{2\pi\ell s_i}{S_{\text{total}}}, \tag{6}$$

which ensures that the total phase variation along the closed contour equals $2\pi\ell$ [4]. Unlike the analytical formulation, the phase accumulation is computed directly from discrete contour coordinates, without requiring contour reconstruction, derivative estimation or numerical integration over a continuous parameter space. Consequently, the computational complexity depends primarily on the number of contour pixels rather than on the reconstruction of an intermediate parametric representation.

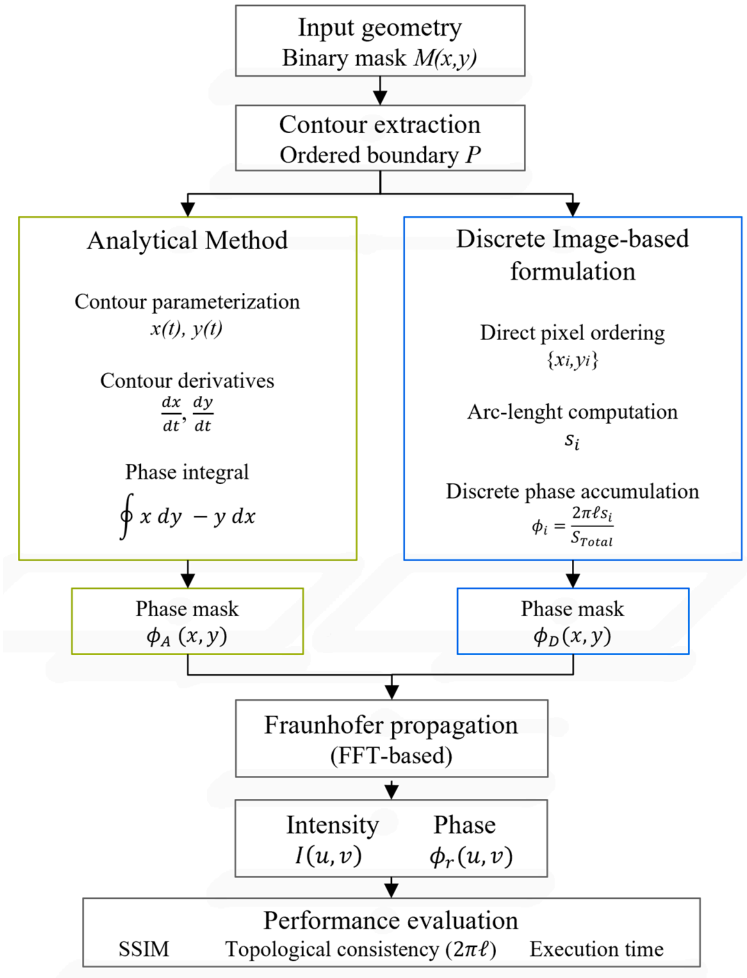

Figure 1. Comparative workflow of analytical and discrete image-based contour hologram synthesis. Both formulations are evaluated under identical computational conditions using structural fidelity, topological consistency, and computational cost metrics.

This discrete formulation preserves the global topological constraint while avoiding explicit evaluation of continuous integrals. The resulting phase values are mapped onto a two-dimensional grid to construct the phase hologram used for numerical propagation. Pixels corresponding to contour locations are assigned the computed phase values, whereas all remaining pixels are set to a zero-phase background. This formulation eliminates the need for contour parameterization, symbolic differentiation, and numerical integration over continuous domains. All operations are performed directly on discrete pixel coordinates, providing a computationally efficient framework for handling arbitrary contour geometries.

The workflow in Figure 1 summarizes the processing stages used by both formulations and highlights the main computational differences considered in the comparative analysis. Since no intermediate Fourier contour reconstruction stage is required in the discrete formulation, local geometric features such as corners, cusps, and abrupt curvature variations are preserved directly in the sampled contour representation.

2.3. Numerical Propagation and Implementation

The phase distributions generated by both formulations are evaluated through numerical propagation under the Fraunhofer approximation. The complex field at the hologram plane is defined as

$$U(x, y) = A(x, y)e^{i\phi(x,y)}, \tag{7}$$

assuming a uniform amplitude, $A(x,y) = 1$, and a spatially varying phase [8]. The far-field distribution is obtained by computing the Fourier transform of the complex field such that the intensity is given by

$$I(u,v) = |\mathcal{F}\{U(x,y)\}|^2, \tag{8}$$

where $\mathcal{F}\{\cdot\}$ denotes the two-dimensional Fourier transform [8]. For all simulations, the wavelength was fixed at $\lambda = 532$ nm. The hologram plane was sampled on a 512×512 grid with a pixel pitch of $\Delta x = \Delta y = 19$ µm. Both formulations are propagated using identical Fourier-based numerical propagation and sampling parameters. Therefore, the observed differences in the reconstructed patterns can be attributed to the contour representation strategy rather than to differences in the propagation model. Since the study is restricted to numerical propagation of deterministic phase masks, no random phase modulation or speckle-reduction procedure was applied.

The coordinate system is centered at the image midpoint to avoid numerical asymmetries in the reconstructed phase patterns. Numerical implementation was carried out in MATLAB R2025b, using FFT-based propagation routines. Both methods were executed under identical computational conditions, including grid size, sampling resolution, and numerical precision, to ensure direct comparability of results. Computational performance was evaluated using a desktop computer equipped with an Intel Core i7-10700T CPU (2.00 GHz) and 16 GB of RAM. No GPU acceleration, parallel computing toolbox, or external hardware acceleration was employed.

2.4. Evaluation Metrics

The performance of both formulations is evaluated using quantitative and qualitative criteria that assess structural fidelity, phase-topology preservation, and computational efficiency. The evaluation metrics considered in this study are summarized in Table 1.

Table 1. Evaluation metrics used for comparative analysis of analytical and discrete image-based formulations.

Metric	Description
SSIM	Structural similarity between reconstructed contour and target geometry
Topological charge consistency	Verification of topological charge preservation
Execution time	Computational cost of phase mask generation

The Structural Similarity Index (SSIM) is computed using edge representations extracted from the reconstructed intensity distributions and the target contours after adaptive binarization and contour extraction [30]. Although metrics such as the Root Mean Square Error (RMSE) and Pearson correlation coefficient are commonly used in image and hologram evaluation, SSIM was selected because the objective of this study is to assess the preservation of contour geometry and local structural features rather than pixel-wise intensity agreement [30]. Since the comparison is performed on contour representations derived from the reconstructed fields, SSIM provides a more meaningful measure of structural fidelity for the present application.

Phase behavior is analyzed by inspecting the continuity and winding of the phase distribution along the contour. In particular, the consistency of the encoded topological charge ℓ is verified by confirming that the total phase variation along the contour equals $2\pi\ell$ [4].

Computational performance is assessed by measuring the hologram generation time required to generate the phase mask for each formulation. The reported values correspond to the complete phase-synthesis procedure, from contour extraction to phase-mask generation, excluding numerical propagation and visualization stages. Generation times were measured over fifteen independent executions for each contour, and the reported results correspond to the mean and standard deviation of the measured execution times.

2.5. Computational Protocol

To ensure a consistent and reproducible comparison, both formulations were evaluated under identical computational conditions. A dataset composed of twelve closed contours was used for evaluation and organized into four categories according to their dominant shape characteristics: smooth, polygonal, cusp-based, and free-form contours. Each category contains three representative geometries, allowing reconstruction fidelity and computational cost to be assessed across different contour families while reducing the influence of any individual shape on the reported results. Figure 2 presents one representative contour from each category, whereas the complete evaluation dataset is shown in Figure 3.

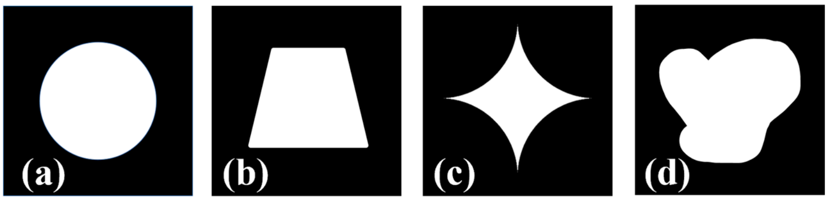

Figure 2. Representative input geometries selected from the four contour categories used for comparative evaluation: (**a**) smooth, (**b**) polygonal, (**c**) cusp-based, and (**d**) free-form contours.

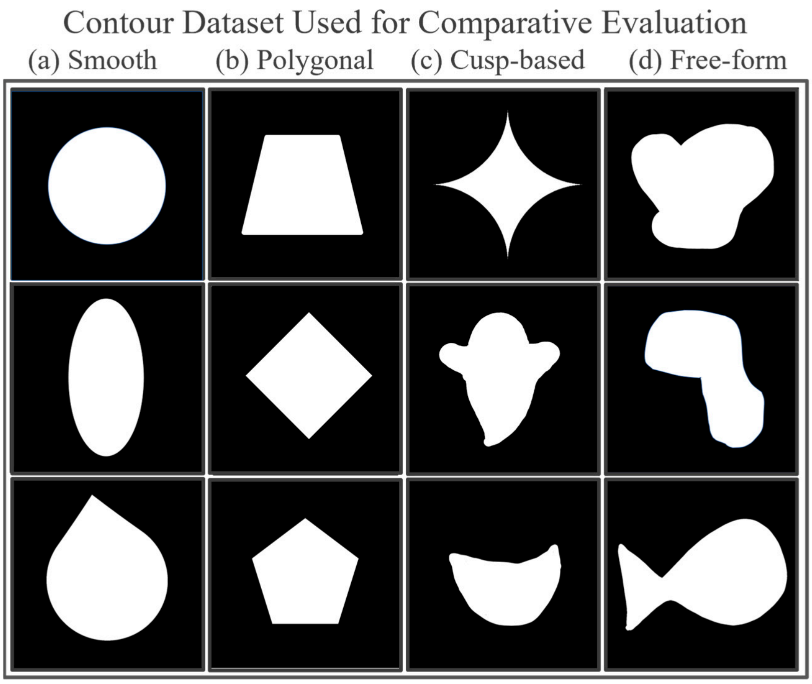

Figure 3. Complete dataset of twelve contours used for evaluation. The geometries are grouped into four categories according to their dominant shape characteristics: (**a**) smooth, (**b**) polygonal, (**c**) cusp-based, and (**d**) free-form contours.

For each input geometry, phase masks were generated using both formulations and evaluated using the metrics described in Section 2.4. Each contour was processed fifteen independent times for each formulation. Results by categories reported in the next section were computed by considering the values from the three contours belonging to each category.

Memory requirements were estimated from the contour representation used by each formulation. For the analytical formulation, memory was computed from the fixed-length Fourier descriptor representation used to reconstruct each contour; therefore, the estimated memory requirement remains constant across contour categories. For the discrete image-based formulation, memory was computed from the stored coordinates of the extracted contour pixels; therefore, this value depends on the number of contour pixels in each geometry.

All simulations were conducted using the same computational environment and parameter configuration, ensuring that differences in performance are attributable solely to the formulation of each method.

3. Results and Discussion

The analytical and discrete image-based formulations described in Section 2 were evaluated using the twelve-contour dataset shown in Figure 3. The comparison focuses on reconstruction fidelity, preservation of topological properties, and computational efficiency across the four contour categories: smooth, polygonal, cusp-based and free-form.

3.1. Qualitative Reconstruction Analysis

The qualitative analysis focuses on the visual inspection of the reconstructed intensity distributions obtained from both formulations. Figure 4 presents the complete set of propagated intensity patterns for the twelve-contour dataset, including the target contours and the corresponding reconstructions obtained with the analytical and discrete image-based formulations.

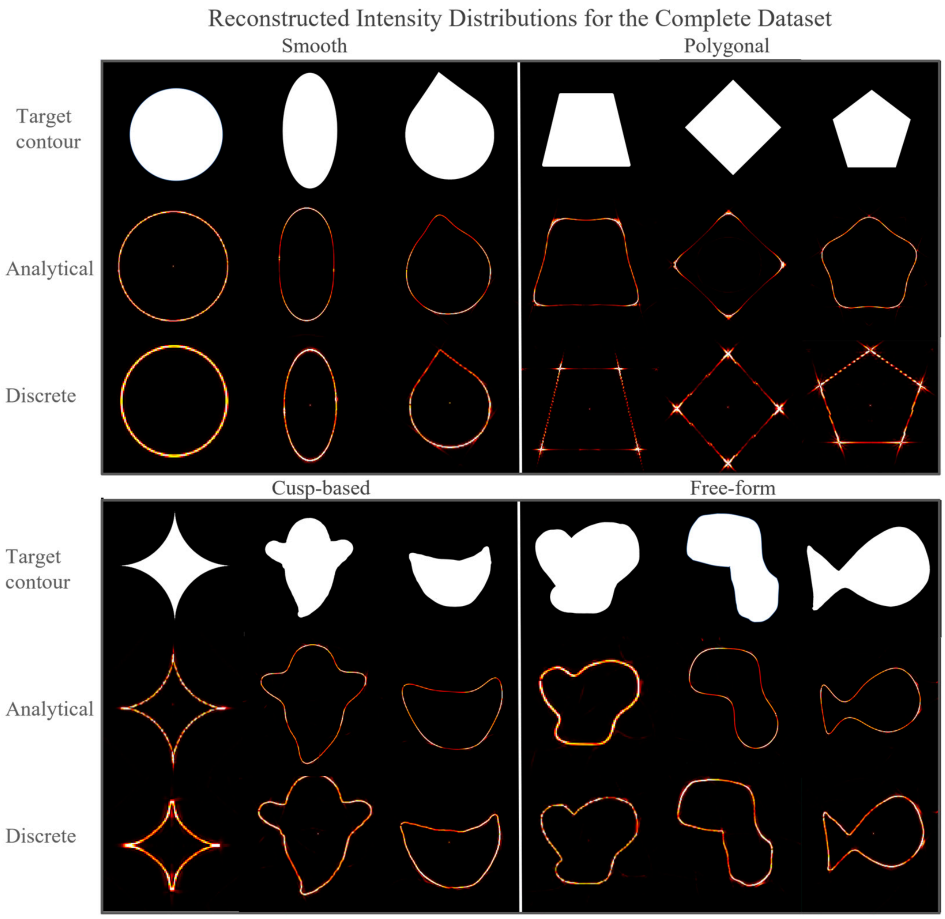

Figure 4. Reconstructed intensity distributions for the complete twelve-contour dataset. Target contours are grouped into smooth, polygonal, cusp-based, and free-form categories, with the corresponding analytical and discrete image-based reconstructions shown for each case.

For smooth geometries, both formulations produce similar reconstructions, preserving the global contour shape and overall continuity. Local differences become more evident as contour complexity increases. In polygonal geometries, the analytical formulation tends to produce smoother transitions and slightly rounded corners, which is associated with the Fourier-based contour reconstruction used in the analytical approach. In contrast, the discrete image-based formulation preserves sharper geometric transitions by operating directly on the sampled contour points.

For cusp-based and free-form contours, both formulations reconstruct the main structure of the target geometries, although local differences appear in regions with abrupt curvature variations or irregular boundaries. These differences are more noticeable in contours with corners, cusps, and rapidly varying curvature. Overall, the complete set of reconstructed intensity patterns confirms that both formulations successfully reconstruct the evaluated contour geometries, while the discrete image-based formulation provides improved preservation of local geometric features across the complete dataset.

3.2. Structural Fidelity Analysis

To quantitatively assess reconstruction fidelity, the SSIM was computed between the target contours and the reconstructed patterns using the procedure described in Section 2.4. Table 2 presents representative SSIM values obtained for one contour from each evaluation category, whereas Table 3 summarizes the category-based statistics computed from the complete twelve-contour dataset using fifteen independent executions per contour and per formulation.

Table 2. Representative SSIM values obtained for one contour from each evaluation category.

	Shape	Analytical	Discrete Image-Based
(a)	Circle	0.936	0.942
(b)	Trapezoid	0.944	0.956
(c)	Asteroid	0.937	0.947
(d)	Free-form contour	0.938	0.945

Table 3. Mean ± standard deviation of SSIM values and average estimated memory requirements for the complete twelve-contour dataset grouped by contour category.

Category	Analytical SSIM	Memory	Discrete SSIM	Memory
Smooth	0.940 ± 0.005	32 KB	0.945 ± 0.003	14 KB
Polygonal	0.940 ± 0.006	32 KB	0.955 ± 0.005	14.4 KB
Cusp-based	0.934 ± 0.005	32 KB	0.950 ± 0.005	13.9 KB
Free-form	0.940 ± 0.006	32 KB	0.950 ± 0.006	15.3 KB

For the representative cases shown in Table 2, both formulations achieved SSIM values above 0.93, indicating strong agreement between the reconstructed and target geometries. The discrete image-based formulation consistently produced slightly higher SSIM values than the analytical formulation. The differences remain relatively small, suggesting that both approaches preserve the global contour structure with high accuracy. The observed differences are associated with the representation strategy used by each formulation. The analytical formulation relies on contour parameterization, numerical differentiation, and Fourier-based reconstruction, which may introduce small local deviations after discretization. In contrast, the discrete image-based formulation operates directly on sampled contour points, improving local contour alignment with the target geometry. This effect is more noticeable in polygonal and cusp-based contours, where abrupt transitions and curvature variations are more sensitive to the contour representation.

Table 3 extends this comparison to the complete dataset by reporting the mean and standard deviation of the SSIM values for the three contours in each category. It also includes the estimated memory requirements associated with the contour representation used by each formulation, reported as average values without standard deviation. For the analytical formulation, the memory requirement remains approximately constant across all categories because the contour is represented using a fixed-length Fourier descriptor vector. In contrast, the memory required by the discrete image-based formulation varies with geometry because the method explicitly stores the coordinates of the extracted contour pixels. In both cases, the memory requirements remain small, indicating that the main difference between the two formulations is associated with computational time rather than storage demand.

Overall, the results presented in Tables 2 and 3 confirm that both formulations achieve high reconstruction fidelity across all contour categories. The discrete image-based formulation provides a slight but consistent advantage in preserving local geometric structures without compromising contour reconstruction.

3.3. Phase Behavior and Topological Consistency

In addition to structural fidelity, the phase behavior of the reconstructed optical field was analyzed to verify the preservation of the encoded topological properties. Figure 5 presents representative phase distributions obtained using the analytical and discrete image-based formulations for one contour from each evaluation category and selected topological charge values. For the fixed charge case, $\ell = 1$, both formulations generate phase distributions with the expected winding behavior around the contour. Smooth geometries, such as the circular contour, exhibit continuous and regular phase evolution in both approaches. Similar global phase behavior is observed for the cusp-based contour, where the characteristic geometry is preserved while maintaining the expected phase topology.

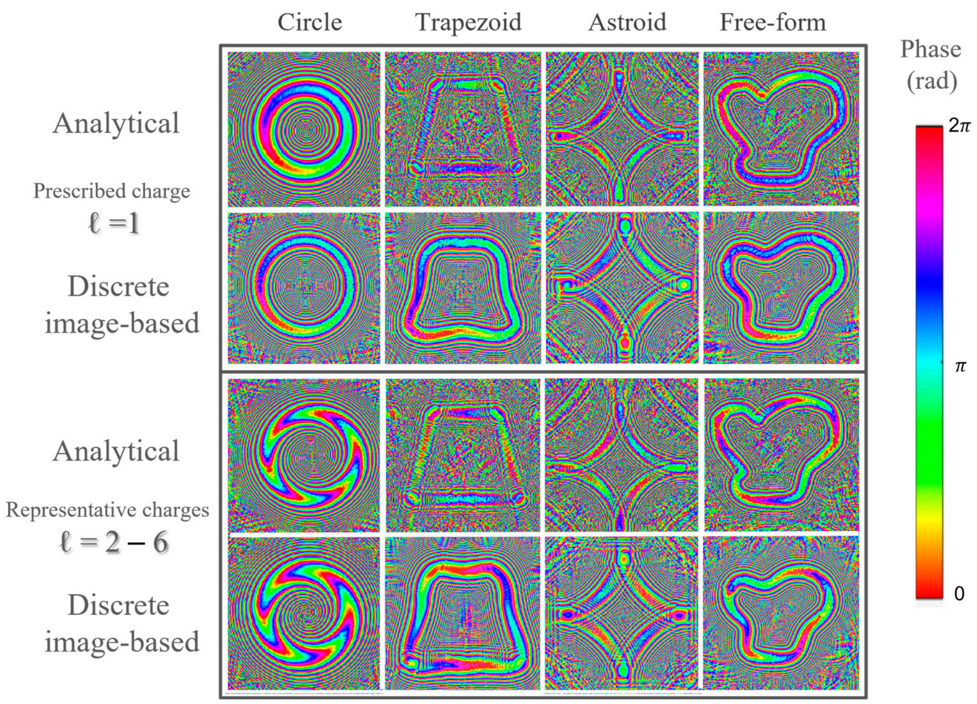

Figure 5. Representative phase distributions generated using the analytical and discrete image-based formulations. One contour from each evaluation category (smooth, polygonal, cusp-based, and free-form) is shown. Upper panels correspond to a prescribed charge $\ell = 1$, whereas lower panels show representative examples for larger charge values.

Local differences become more evident in geometries with abrupt transitions or irregular boundaries, such as the trapezoidal and free-form contours. The analytical formulation tends to produce smoother phase transitions due to contour parameterization and Fourier-based reconstruction. In contrast, the discrete image-based formulation preserves local geometric variations more directly from the sampled contour representation, resulting in sharper local phase transitions near corners and rapid curvature changes.

For larger representative charge values, the phase distributions show the expected increase in phase winding. Despite local differences between both formulations, the global phase topology remains consistent across the evaluated contour categories. These results indicate that both approaches correctly encode the prescribed vortex characteristics, while the discrete image-based formulation provides stronger preservation of local geometric features in contours with higher spatial complexity.

3.4. Computational Cost Analysis

The computational cost was evaluated from the hologram generation time defined in Section 2.4. Table 4 summarizes the mean generation times and speed-up factors obtained for the twelve-contour dataset grouped by contour category, using fifteen independent executions per contour and per formulation.

Table 4. Mean $\pm$ standard deviation of hologram generation times grouped by contour category. Speed-up factors correspond to the ratio between analytical and discrete image-based formulations.

Category	Analytical (s)	Discrete Image-Based (s)	Speed-Up (TA/TD)
Smooth	216 ± 8.0	1.80 ± 0.25	120
Polygonal	469 ± 9.0	1.68 ± 0.30	279
Cusp-based	2099 ± 11.0	1.28 ± 0.23	1639
Free-form	880 ± 8.2	1.72 ± 0.31	511

The results show that the discrete image-based formulation requires substantially less computation time than the analytical formulation for all contour categories. While the discrete method maintains nearly constant execution times between 1.28 s and 1.80 s, the analytical formulation exhibits larger variations, ranging from 216 s for smooth contours to more than 2000 s for cusp-based geometries. The largest speed-up factor is observed for the cusp-based category, where the analytical reconstruction requires a richer Fourier representation to preserve curvature variations and local contour details. This increases the computational burden associated with contour parameterization, derivative estimation, and numerical integration. In contrast, the discrete image-based formulation operates directly on sampled contour coordinates and avoids continuous-domain reconstruction, resulting in a more stable computational cost across contour categories.

As summarized in Table 4, the speed-up factors range from approximately 120$\times$ for smooth contours to more than 1600$\times$ for cusp-based geometries. These results indicate that the computational advantage of the discrete image-based formulation becomes more pronounced when richer contour representations are required, while maintaining the reconstruction fidelity and topological consistency discussed in Sections 3.2 and 3.3.

Since deterministic phase masks were used without random phase modulation, the propagated fields retain coherent diffractive features directly associated with the encoded contour geometry. In particular, sharp edges, corners, cusps, and abrupt curvature variations introduce high spatial frequency components that may lead to diffraction fringes, side lobes, and localized ringing around the reconstructed contour. These effects are more pronounced in polygonal and free-form geometries, where the spatial spectrum contains stronger discontinuities than in smooth contours. The absence of random phase modulation was intentional in this study because it allows the comparison to isolate the effect of contour representation without introducing additional stochastic variations. However, in practical optical implementations, random or optimized phase modulation could be incorporated to redistribute energy and reduce coherent artifacts, although this may also introduce speckle-like intensity fluctuations and would require a separate optimization strategy.

It is also important to clarify that the present formulation is intended for contour-defined targets represented by binary masks or extracted edge maps. Grayscale objects and complex scenes involve spatially varying amplitudes or intensity information and therefore correspond to a different hologram-synthesis problem. Their evaluation would require additional amplitude-encoding or optimization stages beyond the contour-based framework considered here. For this reason, grayscale scene reconstruction is considered a separate extension of the present contour-based framework.

It should be noted that the present comparison is restricted to numerical phase-mask generation and Fraunhofer propagation. In an experimental optical setup with an SLM, factors such as pixelation, phase quantization, alignment errors, and experimental noise may affect the reconstructed intensity distributions. Therefore, future work will include experimental implementation with an SLM to evaluate these effects under laboratory conditions. The present study is not intended to benchmark against general-purpose CGH acceleration methods, but to isolate the effect of contour representation under identical numerical propagation conditions.

4. Conclusions

This work presented a comparative analysis between analytical and discrete image-based formulations for contour hologram synthesis under identical computational conditions. Both approaches were evaluated in terms of structural fidelity, phase behavior, topological consistency, and computational cost using a dataset of twelve contour geometries grouped into smooth, polygonal, cusp-based, and free-form categories.

The results demonstrated that both formulations successfully reconstructed the desired contour geometries while preserving the imposed topological properties of the optical field. Qualitative analysis showed that both approaches maintain the global characteristics of the target structures, while local differences become more noticeable in contours containing abrupt transitions and irregular features. The analytical formulation generally produced smoother contour and phase transitions due to its Fourier-based contour representation, while the discrete image-based formulation preserved local geometric characteristics more directly from the sampled contour representation. Structural similarity analysis revealed high SSIM values for all evaluated geometries, with values exceeding 0.93 in all cases, indicating strong agreement between reconstructed and target contours. Although both formulations achieved comparable reconstruction fidelity, the discrete image-based formulation consistently produced slightly larger similarity values, indicating improved preservation of local contour information while maintaining global shape characteristics. Phase analysis further confirmed that both formulations correctly preserve the imposed topological charge and reproduce the expected phase winding behavior associated with optical vortex fields. While local differences in phase transitions were observed in regions containing high spatial-frequency content, the global phase topology remained consistent across all evaluated geometries and charge values.

The most significant differences were observed in computational cost. The discrete image-based formulation achieved substantial reductions in hologram generation time, with speed-up factors ranging from approximately $120\times$ for smooth contours to more than $1600\times$ for cusp-based geometries when averaged across the complete evaluation dataset. In contrast, the computational cost of the analytical formulation increased significantly with contour complexity, whereas the discrete formulation maintained nearly constant generation times across all evaluated cases.

Overall, the results demonstrate that the discrete image-based formulation provides an efficient and flexible alternative for contour hologram synthesis, combining high reconstruction fidelity, preservation of topological properties, and significantly reduced computational requirements. These results indicate that discrete image-based contour representations provide a scalable alternative to analytical contour parameterizations for hologram synthesis involving arbitrary geometries and increasing contour complexity.

Author Contributions: Conceptualization, A.S.-T.; methodology, A.S.-T. and J.J.E.-E.; software, A.S.-T.; validation, A.S.-T. and D.A.T.-T.; formal analysis, A.S.-T. and L.J.-B.; investigation, D.A.T.-T. and L.J.-B.; resources, A.S.-T.; data curation, J.J.E.-E.; writing—original draft preparation, A.S.-T.; writing—review and editing, J.J.E.-E., D.A.T.-T. and L.J.-B.; visualization, A.S.-T.; supervision, A.S.-T.; project administration, A.S.-T. All authors have read and agreed to the published version of the manuscript.

Funding: This research received no external funding.

Institutional Review Board Statement: Not applicable.

Informed Consent Statement: Not applicable.

Data Availability Statement: The datasets generated during this study are not publicly available because they consist of research-stage computational implementations and simulation outputs used for methodological development but are available from the corresponding author upon reasonable request.

Acknowledgments: During the preparation of this manuscript, the authors used ChatGPT based on GPT-5.5 Thinking (OpenAI) for language refinement and manuscript organization. The authors reviewed and edited all generated content and take full responsibility for the final content of this publication.

Conflicts of Interest: The authors declare no conflicts of interest.

References

1. Forbes, A.; de Oliveira, M.; Dennis, M.R. Structured light. *Nat. Photonics* **2021**, *15*, 253–262. [CrossRef]
2. Rubinsztein-Dunlop, H.; Forbes, A.; Berry, M.V.; Dennis, M.R.; Andrews, D.L.; Mansuripur, M.; Denz, C.; Alpmann, C.; Banzer, P.; Bauer, T.; et al. Roadmap on structured light. *J. Opt.* **2017**, *19*, 013001. [CrossRef]
3. Wang, J.; Li, K.; Quan, Z. Integrated structured light manipulation. *Photonics Insights* **2024**, *3*, R05. [CrossRef]
4. Shen, Y.; Wang, X.; Xie, Z.; Min, C.; Fu, X.; Liu, Q.; Gong, M.; Yuan, X. Optical vortices 30 years on: OAM manipulation from topological charge to multiple singularities. *Light Sci. Appl.* **2019**, *8*, 90. [CrossRef] [PubMed]
5. Rosales-Guzmán, C.; Forbes, A. *How to Shape Light with Spatial Light Modulators*; SPIE Press: Bellingham, WA, USA, 2017.
6. Soshnikov, D.V.; Doskolovich, L.L.; Motz, G.A.; Byzov, E.V.; Bezus, E.A.; Bykov, D.A.; Mingazov, A.A. Design of cascaded diffractive optical elements. *Photonics* **2023**, *10*, 766. [CrossRef]
7. Bhattacharya, S.; Vijayakumar, A. *Design and Fabrication of Diffractive Optical Elements*; SPIE Press: Bellingham, WA, USA, 2017.
8. Voelz, D.G. *Computational Fourier Optics*; SPIE Press: Bellingham, WA, USA, 2011.
9. Chen, L.; Zhang, H.; Cao, L.; Jin, G. Non-Iterative Phase Hologram Generation with Optimized Phase Modulation. *Opt. Express* **2020**, *28*, 17436–17452. [CrossRef] [PubMed]
10. Velez-Zea, A.; Barrera-Ramírez, J.F. Non-Iterative Phase-Only Hologram Generation. *Photonics* **2025**, *12*, 500. [CrossRef]
11. Liu, S.; Takaki, Y. Optimization of Phase-Only Computer-Generated Holograms Based on the Gradient Descent Method. *Appl. Sci.* **2020**, *10*, 4283. [CrossRef]
12. Blinder, D.; Schelkens, P. Fast Low-Precision Computer-Generated Holography on GPU. *Appl. Sci.* **2021**, *11*, 6235. [CrossRef]
13. Wang, Y.; Zhang, H.; Fan, H.; Qin, W.; Poon, T.-C. Fast Polygon-Based Computer-Generated Holography Using Lookup Tables and Principal Component Analysis. *Opt. Express* **2021**, *29*, 35442–35458. [CrossRef] [PubMed]
14. Liu, K.; Wu, J.; Cao, L. High-quality and high-speed computer-generated holography via deep-learning-assisted bidirectional error diffusion method. *Opt. Express* **2024**, *32*, 37342–37354. [CrossRef] [PubMed]
15. Peng, Y.; Choi, S.; Padmanaban, N.; Wetzstein, G. Neural holography with camera-in-the-loop training. *ACM Trans. Graph.* **2020**, *39*, 185. [CrossRef]
16. Yu, X.; Zhang, H.; Zhao, Z.; Fan, X.; Hu, S.; Li, Z.; Gao, H. On the Use of Deep Learning for Computer-Generated Holography. *iScience* **2025**, *28*, 112507. [CrossRef] [PubMed]

17. Georgieva, A.; Belashov, A.V.; Petrov, N.V. Optimization of DMD-Based Independent Amplitude and Phase Modulation by Analysis of Target Complex Wavefront. *Sci. Rep.* **2022**, *12*, 7754. [CrossRef] [PubMed]
18. Zhang, Y.; Fan, H.; Wang, F.; Gu, X.; Qian, X.; Qin, W.; Fu, Q.; Poon, T.-C. Polygon-Based Computer-Generated Holography: A Review of Fundamentals and Recent Progress. *Appl. Opt.* **2022**, *61*, B363–B389. [CrossRef] [PubMed]
19. Fan, H.; Zhang, Y.; Wang, F.; Qin, W.; Fu, Q.; Poon, T.-C. Fast 3D Analytical Affine Transformation for Polygon-Based Computer-Generated Holograms. *Appl. Sci.* **2022**, *12*, 6873. [CrossRef]
20. Wang, Y.; Dong, D.; Christopher, P.J.; Kadis, A.; Mouthaan, R.; Yang, F.; Wilkinson, T.D. Hardware implementations of computer-generated holography: A review. *Opt. Eng.* **2020**, *59*, 102413. [CrossRef]
21. Li, J.; Jabbireddy, S.; Zhang, Y.; Metzler, C.A.; Varshney, A. Instant-SFH: Non-Iterative Sparse Fourier Holograms Using Perlin Noise. *Sensors* **2024**, *24*, 7358. [CrossRef] [PubMed]
22. Magallón, J.A.; Blesa, A.; Serón, F.J. Monte-Carlo Techniques Applied to CGH Generation Processes and Their Impact on the Image Quality Obtained. *Eng. Rep.* **2025**, *7*, e13109. [CrossRef]
23. McWilliam, R.; Williams, G.L.; Cowling, J.J.; Seed, N.L.; Purvis, A. High-contrast pattern reconstructions using a phase-seeded point CGH method. *Appl. Opt.* **2016**, *55*, 1703–1712. [CrossRef] [PubMed]
24. Rodrigo, J.A.; Alieva, T.; Calvo, M.L. Shaping Light Beams along Curves. *Opt. Express* **2013**, *21*, 20544–20555. [CrossRef] [PubMed]
25. Gao, Z.; Voronine, D.V.; Sokolov, A.V. Plasmonic vortices: A promising tool utilizing plasmonic orbital angular momentum. *Photonics* **2025**, *12*, 125. [CrossRef]
26. Swan, H.; Torchylo, A.; Van de Graaff, M.J.; Rudolph, J.; Hogan, J.M. High-fidelity holographic beam shaping with optimal transport and phase diversity. *Opt. Express* **2025**, *33*, 6290–6303. [CrossRef] [PubMed]
27. González, R.C.; Woods, R.E. *Digital Image Processing*, 4th ed.; Pearson: New York, NY, USA, 2018.
28. Cristóbal, G.; Schelkens, P.; Thienpont, H. *Optical and Digital Image Processing*; Wiley: Hoboken, NJ, USA, 2011.
29. Serrano-Trujillo, A.; Ruiz-Cortés, V. Encoding Intensity and Phase Gradient. *Appl. Sci.* **2023**, *13*, 3192. [CrossRef]
30. Wang, Z.; Bovik, A.C.; Sheikh, H.R.; Simoncelli, E.P. Image Quality Assessment: From Error Visibility to Structural Similarity. *IEEE Trans. Image Process.* **2004**, *13*, 600–612. [CrossRef] [PubMed]
31. Xu, X.; Zhang, Z.; Liu, Y.; Wang, Y. Efficient Computer-Generated Holography Based on Mixed Linear Convolutional Neural Networks. *Appl. Sci.* **2022**, *12*, 4177. [CrossRef]
32. Minikhanov, R.; Shoykhetbrod, A.; Kozlov, S. Computer-Generated Holography Methods for Data Page Reconstruction Using Phase-Only Medium. *Appl. Sci.* **2023**, *13*, 4479. [CrossRef]

https://doi.org/10.3390/app16146890